J. Fluid Mech. (1983), *vol.* 126, *pp.* 251–268
Printed in Great Britain

On characteristics of the water-particle velocity in a plunging breaker

By TAKEO NAKAGAWA

Department of Civil Engineering, Kanazawa Institute of Technology, Nonoichi, Kanazawa 921 Japan

(Received 10 February 1982)

Three velocity components of water particles in a plunging breaker over a horizontal step on the bed of a two-dimensional laboratory wave tank have been determined simultaneously by means of an elaborate flowmeter that measures the flow drag on three 'tension threads', with each recording a separate flow component.

It is found that all three of the r.m.s. values in the plunging breaker become maximum at $x/L \approx 0{\cdot}7$, where x is the distance from the breaking point to the shore and L is the wavelength. It is found that both the velocity and r.m.s. values of the transverse flow component generated by the shoaling and wave breaking become comparable to those of the other two flow components.

On the basis of spectral analyses it is found that major wave frequencies in both the longitudinal and vertical flow components of the original two-dimensional wave survive even after experiencing relatively strong shoaling and wave breaking, and part of the original wave energy is transferred to the transverse flow component and is located at these major frequencies. It is found that the majority of the higher-harmonic-frequency components (or turbulent fluctuations) are generated in the shoaling process and that the wave breaking provides a relatively minor contribution to the generation. Finally, it is found that, through the shoaling and wave breaking, the original wave energy is transported to a frequency range lower than the primary wave frequency (*negative cascade*), as well as to the higher frequency range (*positive cascade*) in each flow component.

1. Introduction

Nothing perhaps is more elegant than breaking waves accompanied by white foam in coastal locations. Breaking waves and their development are therefore topics that have attracted many researchers, but much remains to be done before a satisfactory understanding is obtained and real prediction is possible.

From visual observations in a laboratory or a surf zone, it appears that immediately after the wave starts to turn over from the breaking point a drastic transition takes place over a horizontal distance of several times the water depth at the breaking point. In this zone the motion still shows large-scale patterns that are repeated with relatively small variations from wave to wave. As the wave propagates further towards the shore, the large-scale deterministic flow breaks up into small-scale fragments, which generally have a random turbulent nature. During this process, *at least*, the appearance of the wave becomes very similar to that of a moving bore, and it normally extends to the shoreline, where the wave run-up starts. This may be the main reason why breaking waves are sometimes modelled by solitary waves (Horikawa & Kuo 1966), bores (Peregrine & Svendsen 1978) or wakes (Battjes & Sakai 1981).

It must be noted, however, that breaking waves are oscillatory waves, while solitary waves, bores and wakes are all translatory waves in which there is a significant transport of fluid particles in the direction of propagation. Thus these tentative modellings cannot be valid in this basic respect.

Workers have recently been able to describe theoretically, in part, the water motions in a wave as it is about a break (e.g. Longuet-Higgins & Cokelet 1976), but it is impracticable to make a highly detailed theoretical analysis of breaking waves worthwhile. Experimental study has progressed slowly owing to problems encountered in modelling the surf zone properly in a laboratory, and in making direct field measurements of the water particle velocity. In the laboratory, water-particle velocities in breaking waves have been measured by Iversen (1952) and Morison & Crooke (1953) using neutrally buoyant particles. The latter study has shown that the greatest horizontal water-particle velocity occurs when the wave is breaking and that there is a differential between the onshore and offshore velocities. Adeyemo (1970) has measured the velocity field near breakers with hydrogen bubbles and has discussed the asymmetry of wave profile and velocity. Battjes & Sakai (1981) have recently measured the velocity field in a steady spilling-type breaker with a laser-Doppler velocimeter. In the surf zone, the water-particle velocities have been measured with instruments such as acoustic and electromagnetic flowmeters (Miller & Ziegler 1964), propellers (Walker 1969), dye tracers (Wood 1973), electromagnetic flowmeters (Führböter & Büsching 1974; Thornton 1968; Steer 1972; Thornton & Richardson 1974; Bub 1974; Galvin 1975; Thornton *et al.* 1976). However, no accurate three-dimensional velocity measurements of water particles have been made, and water-particle velocity measurements have normally been limited to the longitudinal and vertical components. In addition to this major deficiency, the measurements using neutrally buoyant particles and hydrogen bubbles only provide qualitative information. The electromagnetic flowmeter has the main disadvantage of large bulk at the point of measurement. Hot wires are too sensitive to contamination by inevitable impurities in the water and to variation in the ambient temperature. Small propellers are of low sensitivity and low accuracy.

In the present paper, therefore, three velocity components of water particles in a plunging breaker over the horizontal step on the bed of a two-dimensional laboratory wave tank have been determined simultaneously by means of an elaborate flowmeter measuring the flow drag on three 'tension threads', with each recording a separate flow component. The present flowmeter, to be described below, is designed to compensate for the deficiencies of existing flowmeters mentioned above. Nakagawa, Iwata & Koyama (1981) and Nakagawa (1982*a*, *b*) have in fact demonstrated that the present flowmeter is superior to the other flowmeters when it is used to measure water-particle velocities having a three-dimensional and oscillatory nature. The present paper also describes the apparatus and methods of the experiment and data analysis. These are followed by a presentation and discussion of the main results associated with the water-particle velocity, power-spectral density and coherence.

2. Apparatus

Figure 1 shows a schematic diagram of the experimental set-up. The two-dimensional wave tank is 0·7 m wide. The wave generator is a hybrid type of piston and flap. Figure 2 shows a general view of the 'tension-thread' flowmeter. The flow velocity is measured by the three cotton threads [1], [2] and [3], which measure velocities in the x-, y- and z-directions respectively. The cross-sections of the elastic

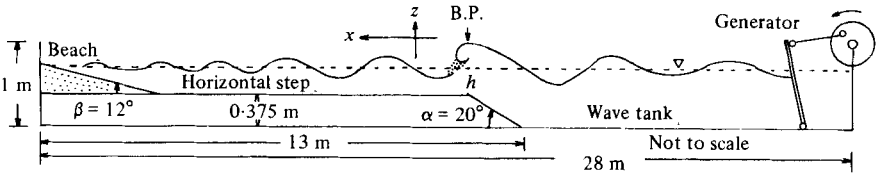

FIGURE 1. Schematic diagram of the experimental set-up.

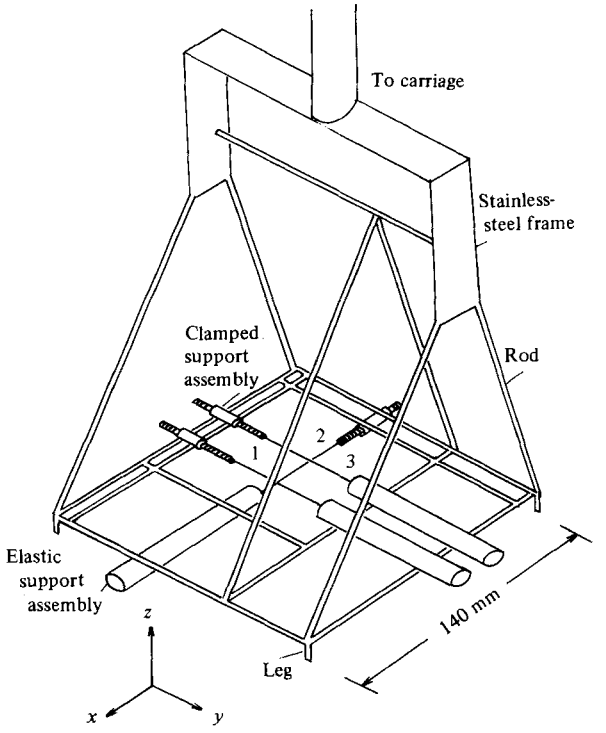

FIGURE 2. General view of the 'tension-thread' flowmeter.

support assembly through the pipe axis are shown in figure 3. The upper cross-section includes the plane of the cantilever of thickness 0·5 mm, whereas the lower cross-section is normal to the plane. One end of the thread is fixed rigidly to the head of the screw rod, while the other end is knotted at the free end of the cantilever so that it is supported elastically. Initial tension in the thread is controllable within a certain limit by adjusting the horizontal position of the screw rod. A semiconductor strain gauge of 120 Ω is glued on each surface of the cantilever, which is made of carbon-fibre-reinforced plastic of specific weight 1·7 and Young modulus $1{\cdot}96 \times 10^5$ N/mm^2. The length and diameter of all the threads are 55 mm and 0·1 mm respectively. Threads [1] and [3] are suspended in the same horizontal plane, and are parallel and separated by 20 mm. Thread [2] is in a horizontal plane at 15 mm below the plane including threads [1] and [3], but it is normal to them. It is therefore clear that the velocity measured by the flowmeter is an integrated mean velocity in the small space where the three threads are suspended; in the data analysis, however, the geometrical centre of the three midpoints of the threads is assumed as the measuring point.

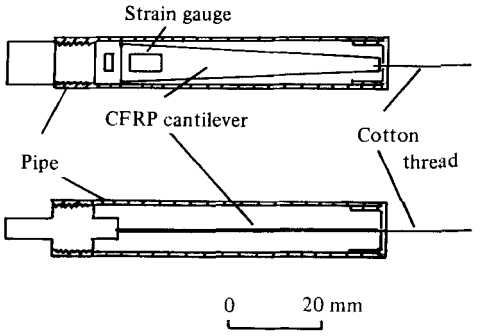

FIGURE 3. Cross-sections of the elastic support assembly.

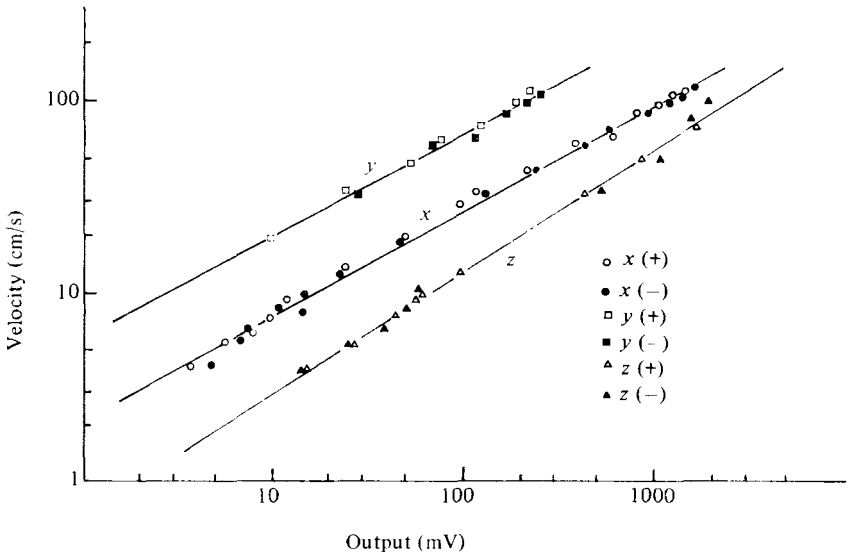

FIGURE 4. Velocity calibration curves.

An increase of the thread tension due to the flow produces a deflection of the cantilever and thus a strain in the gauges. Each of the threads can measure a separate velocity component normal to the plane of the cantilever because the ratio of the width to the thickness is sufficiently large: the ratio is 6 and 16 at the tip and base, of the cantilever respectively. In general, the flow drag on a thread is not proportional to the velocity. It is found, however, that the out-of-balance electrical signal caused by the strain in the cantilever is proportional to the flow velocity when the voltage of the output signal is smaller than a critical value. In the present measurement, only this linear range is used.

Two strain gauges glued to the surface of a cantilever and a bridge box constitute a a.c. Wheatstone bridge, and the out-of-balance electrical signal is amplified by a dynamic amplifier and then recorded on magnetic tape. The analog record on the tape is digitized at the sampling frequency of 50 Hz in the data analysis. It is found by the forced-oscillation test that the natural frequency of the dynamic system of the present flowmeter is approximately 100 Hz. It is impossible, however, to avoid

Parameter \ Position	1 m behind the wave generator	At the wave-breaking point
Wave height H (cm)	10·7	12·7
Wave period T (s)	1·4	1·4
Wavelength L (cm)	—	186·0
Water depth h (cm)	56·5	19·5

TABLE 1. Wave parameters of the plunging breaker

completely some effects on the flow due to the rigs placed in it. These have been minimized by using circular rods of small diameter (5 mm) for the frame and by adopting a design criterion such that each flow component is not disturbed by any rod, insofar as the flow is normal to the plane of the cantilever, at the free end of which the thread is fixed.

Calibrations of the present flowmeter have been made in a tank filled with still water. The plane of the cantilever is carefully set normal to the longitudinal axis of the tank. The flowmeter is towed along the axis at a specified speed in the water and the output electrical signal is then recorded on the tape. In this way, the flowmeter has been calibrated in the velocity range 3·0–120 cm/s. Figure 4 shows the calibration curves, where x, y and z denote the calibration curves for threads [1], [2] and [3] respectively. The open and filled symbols show positive and negative directions respectively.

For a more detailed description of the present flowmeter see Nakagawa *et al.* (1981) and Nakagawa (1982*a*, *b*).

3. Method

3.1. *Experiment*

The supporting rod of the flowmeter is fixed to a point gauge mounted on the carriage, which is capable of moving along the parallel rails on the upper edges of the wave tank. The vertical position of the flowmeter is thus adjusted by turning the point gauge knob. It is therefore possible to change the measuring point in both longitudinal and vertical directions. However, the transverse position is always in the vertical cross-section including the longitudinal central axis of the tank. During measurements of the water-particle velocity, time histories of the water-surface elevation have been obtained with two capacitance-type wave gauges simultaneously. Water-surface elevations are measured 1·0 m behind the wave generator and at the same longitudinal position where the water particle velocity is measured.

The present wave parameters are summarized in table 1, where the wavelength L is calculated from the dispersion relation of the small-amplitude wave theory. Figure 5 shows a photograph of the present plunging breaker when the falling jet from the crest of the wave just starts to break. After the wave has broken, only a small number of air bubbles are entrained into the water in this case, so that it is considered that these bubbles will not seriously affect the performance of the flowmeter. The measuring points for the water-particle velocity range over 9·0 m in the longitudinal direction, and from 2·0 cm above the horizontal step (or tank bed) to 2·0 cm below the wave trough in the vertical direction. Intervals between the measuring points

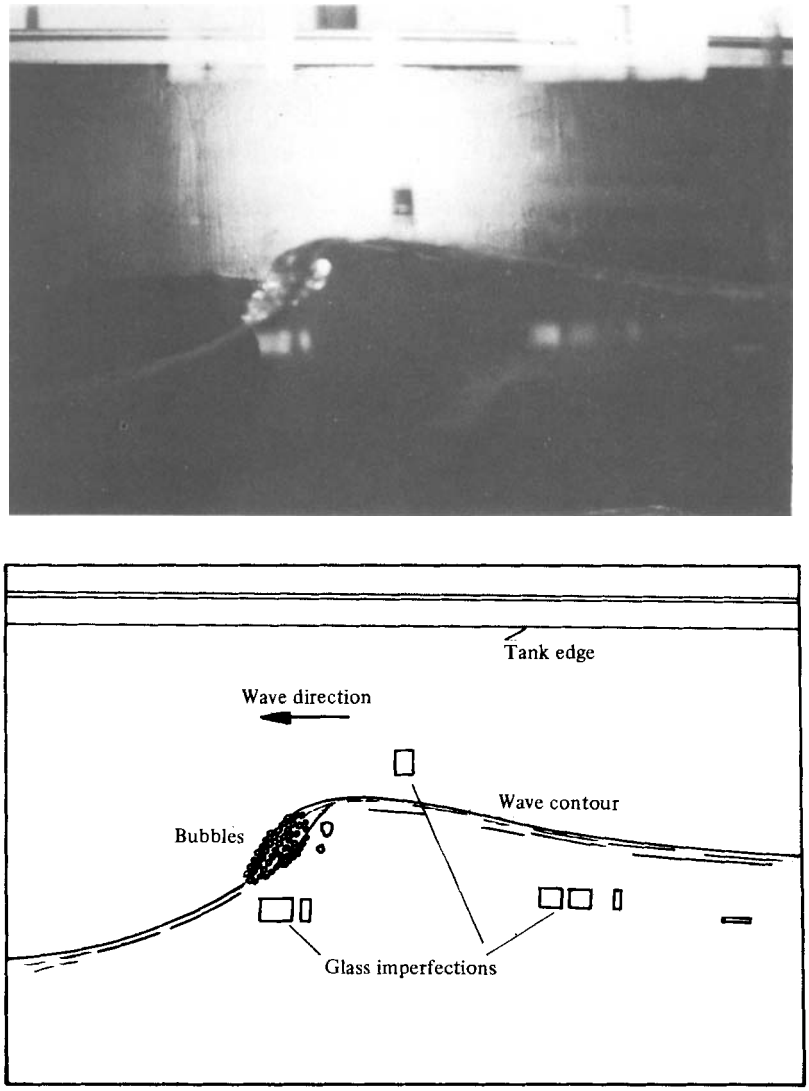

FIGURE 5. Photograph and diagram of the plunging breaker.

in the longitudinal direction and in the vertical direction are 10·0 cm and 2·0 cm respectively. Before any measurements are taken, a time of nearly 10 min is allowed to elapse in order to let the flow develop and establish a quasi-state of the wave.

3.2. *Data analysis*

The water-particle velocities (u, v, w) are first separated into the steady flows (U, V, W) and the unsteady flows $(\hat{u}, \hat{v}, \hat{w})$. Then the unsteady flows are divided into the periodic flows $(\dot{u}, \dot{v}, \dot{w})$ and the turbulent fluctuations (u', v', w'). The unsteady flows in turn are analysed to obtain the power spectrum and the coherence with the water surface elevation. The turbulent fluctuations are analysed to obtain the r.m.s. values.

Steady flow and unsteady flow. The steady flows (U, V, W) are defined as the displaced distances of the water particle per wave period, viz the mass-transport velocity. Therefore the unsteady flows are obtained as $(\hat{u}, \hat{v}, \hat{w}) = (u-U, v-V, w-W)$.

Turbulent fluctuation. There is at present no appropriate definition of the turbulent fluctuation of the water-particle velocity in a breaking wave. It is, however, clear that, once the periodic flows are obtained by a certain way, the turbulent fluctuations may be defined by $(u', v', w') = (\hat{u}-\dot{u}, \hat{v}-\dot{v}, \hat{w}-\dot{w})$.

Two tentative methods are therefore proposed herein in order to define the periodic flows (or turbulent fluctuations). The first is the 'phase-average method', in which a periodic-flow component at a phase is defined by the arithmetic average of a number of unsteady-flow component velocities at the phase in several successive waves. Repetition of this procedure at each phase provides the periodic flows over the full phase of 360°. Once the periodic flows are obtained, it becomes possible to obtain a turbulent fluctuation at a phase as the difference between the unsteady-flow component and the periodic-flow component at the phase. In this analysis, five successive waves are used in order to obtain the periodic flows, and also the r.m.s. values at a point in the wave. The second is the 'moving-average method', in which an periodic-flow component at a given time is defined by a weighted mean of a number of successive unsteady-flow component velocities, separated at a time interval in one wave. In this analysis, the time record of one wave is first digitized at 0·02 s intervals and then a periodic-flow component $\dot{u}_i$ in the x-direction at a time $t = i$, for example, is defined by

$$\dot{u}_i = \tfrac{1}{4}(\hat{u}_{i-1} + 2\hat{u}_i + \hat{u}_{i+1}),$$

where $\hat{u}_{i-1}$, $\hat{u}_i$ and $\hat{u}_{i+1}$ are unsteady-flow component velocities in the x-direction at $t = i-1$, $t = i$ and $t = i+1$ respectively. In a similar way to the phase-average method, a turbulent fluctuation at a time can be obtained as the difference between the unsteady-flow component and the periodic-flow component at the time. In this analysis, five successive waves are used to obtain the r.m.s. values at a point in the wave.

Power-spectral density. The power-spectral density of unsteady flows is calculated by digital cosine transformation of the autocorrelation function (Blackman & Tukey 1958), where the data numbers are 512, lag numbers 200 and degrees of freedom 5. The coherence between the water-surface elevation and unsteady flow component is also calculated using the same method.

4. Result

Steady flow. Figure 6 shows the spatial distribution of the steady flow in the vertical cross-section including the longitudinal central axis of the tank, where the abscissa is the normalized distance x/L from the breaking point, and the ordinate is the distance $(h+z)/h$ normalized by the water depth at the breaking point. It may be noted in figure 6 that the water mass in the upper water layer is transported from the breaking point in both onshore and offshore directions, whereas it seems to be transported from the shore to the breaking point along the horizontal step. However, it may not be possible to establish any definite direction for the steady flows around the wave-breaking point. Note that the inserted scale for U and W is normalized by the longwave celerity $(gh)^{\frac{1}{2}}$.

Unsteady flow. Figure 7 shows time histories of the water-surface elevation η and the unsteady flows $(\hat{u}, \hat{v}, \hat{w})$ at $x/L = -1{\cdot}0$. Referring to figure 6, it is clear that the wave at this position has not yet experienced both shoaling and wave breaking, so it may be considered that the wave at this position is, in practice, the same as the original wave. This assumption will be justified by the results of spectral analyses, to be shown below. Indeed, it may be seen in figure 7 that the wave profiles are almost sinusoidal, with small deformations. Near the water surface, as shown in figure 7(*c*),

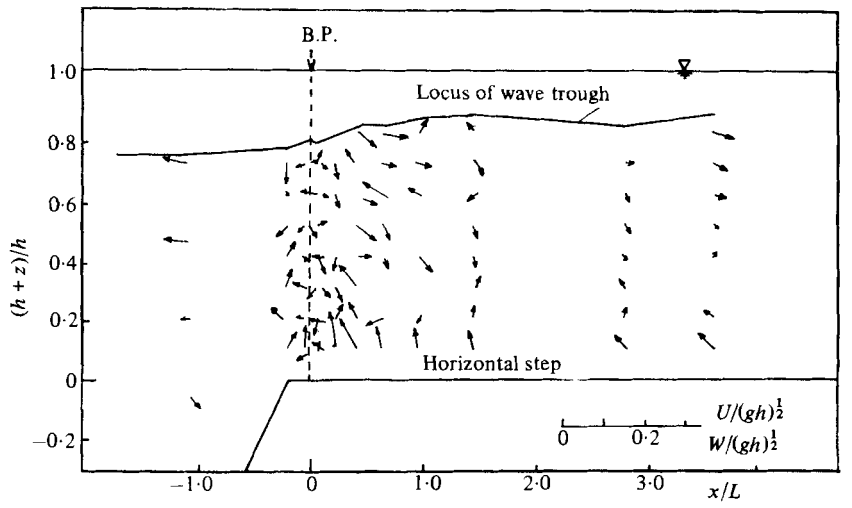

FIGURE 6. Spatial distribution of the steady flow in the vertical cross-section including the longitudinal central axis of the tank.

the phase of η is highly correlated with that of $\hat{u}$ and $\hat{w}$, but is little correlated with that of $\hat{v}$. Near the bed, however, as shown in figures 7 (*a*, *b*), $\eta\hat{w}$-correlation as well as $\eta\hat{v}$-correlation becomes small, though $\eta\hat{u}$-correlation remains large. Figure 8 shows time histories of η, $\hat{u}$, $\hat{v}$ and $\hat{w}$ at the breaking point. At this position, whether the vertical position is near the water surface or not, only $\eta\hat{u}$-correlation is large. It must be noted that through the wave-shoaling process the maximum velocity of $\hat{u}$ becomes almost twice that of the wave at $x/L = -1{\cdot}0$, and the wave profiles become steep and cusplike in shape. Figure 9 shows time histories of η, $\hat{u}$, $\hat{v}$ and $\hat{w}$ at $x/L = 1{\cdot}0$. At this position, similarly to those at the breaking point, only $\eta\hat{u}$-correlation is large and the wave profiles are steep and cusplike in shape. However, through the wave-breaking process, the maximum velocity of $\hat{u}$ this time decreases, and becomes almost the same as that of the wave at $x/L = -1{\cdot}0$.

Turbulent fluctuation. Figure 10 shows how all three r.m.s. values in the plunging breaker depend upon the normalized distance x/L from the breaking point. In the case of the phase-average method, all the r.m.s. values increase from $x/L \approx -0{\cdot}77$ to 0·7. It is almost certain that the increase is due to either the shoaling or wave breaking, but the spectral analyses, to be described, indicate that the major cause is shoaling, and wave breaking provides a relatively minor contribution to it. All the three r.m.s. values, however, decrease from $x/L \approx 0{\cdot}7$ to 1·7 and then seem to approach the respective constant value.

The r.m.s. value in the x-component behaves very similarly to that in the z-component, though the former is smaller than the latter initially, but exceeds it near the breaking point. On the one hand, the r.m.s. value in the y-component is largest initially and becomes comparable to the other two r.m.s. values in the range $0 \lesssim x/L \lesssim 1{\cdot}0$. This value, however, becomes the smallest further downstream.

In the case of the moving-average method, all three r.m.s. values increase from $x/L \approx -0{\cdot}77$ to 0·7. These decrease from $x/L \approx 0{\cdot}7$ to 1·7 and then to approach the respective constant value. The r.m.s. value in the x-component behaves very similarly to that in the z-component, but the r.m.s. value in the y-component is always the largest among them.

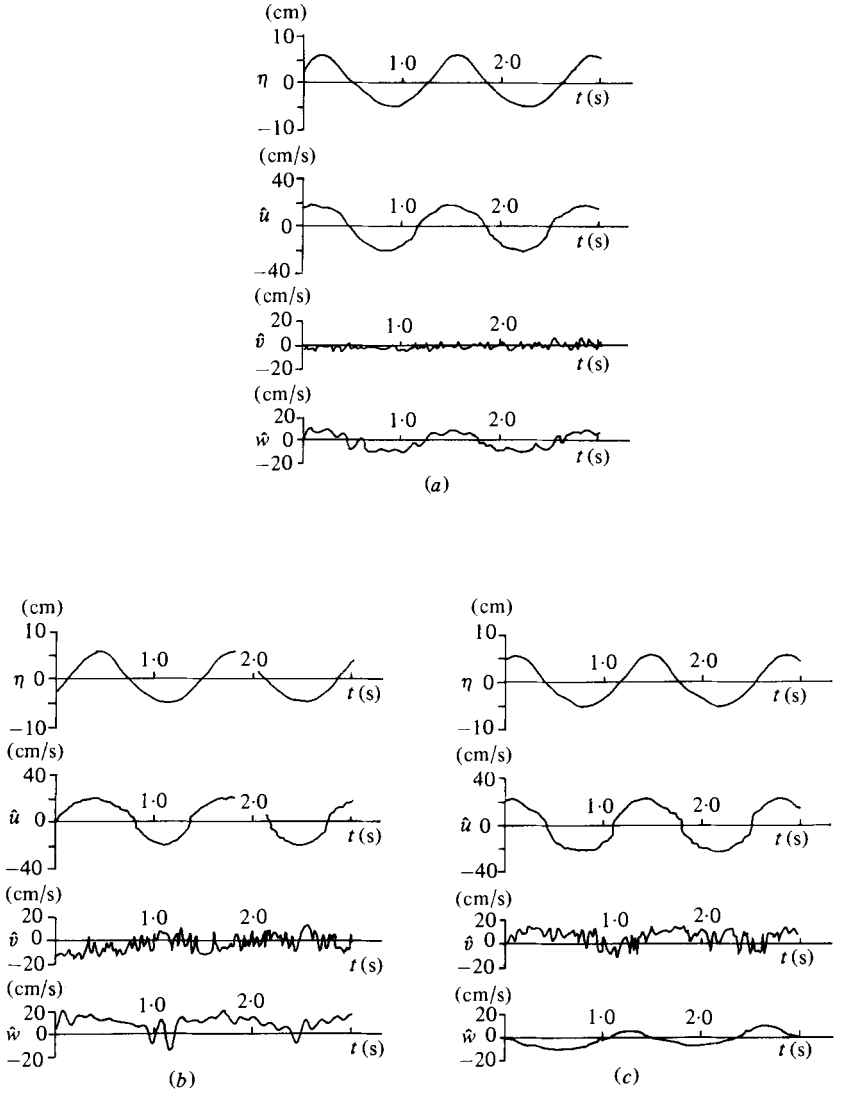

FIGURE 7. Time histories of η, $\hat{u}$, $\hat{v}$ and $\hat{w}$, before shoaling and wave breaking: (*a*) 2 cm above the tank bed; (*b*) 8 cm above the tank bed; (*c*) 2 cm below the wave trough.

Power-spectral density. Figures 11 (*a*, *b*) show respectively the power spectra of the water-surface elevation η 1·0 m behind the wave generator and at $x/L = -1{\cdot}0$ respectively. Note that the latter is a position in front of the horizontal step, so that the wave has not yet experienced the shoaling there. It is clear that both power spectra are very similar to each other, although the latter spectrum contains a little more energy at the higher frequencies. This indicates that any influence of the wave-tank boundary layers on the wave motions in the offshore flow region, viz $x/L \lesssim -1{\cdot}0$, is insignificant compared with the dynamics of the shoaling and wave breaking. Thus it may be justifiable to assume that the wave at $x/L = -1{\cdot}0$ is almost the same as the original wave just behind the wave generator.

Figure 12 shows power spectra of $\hat{u}$, $\hat{v}$ and $\hat{w}$ at 2 cm below the wave trough and

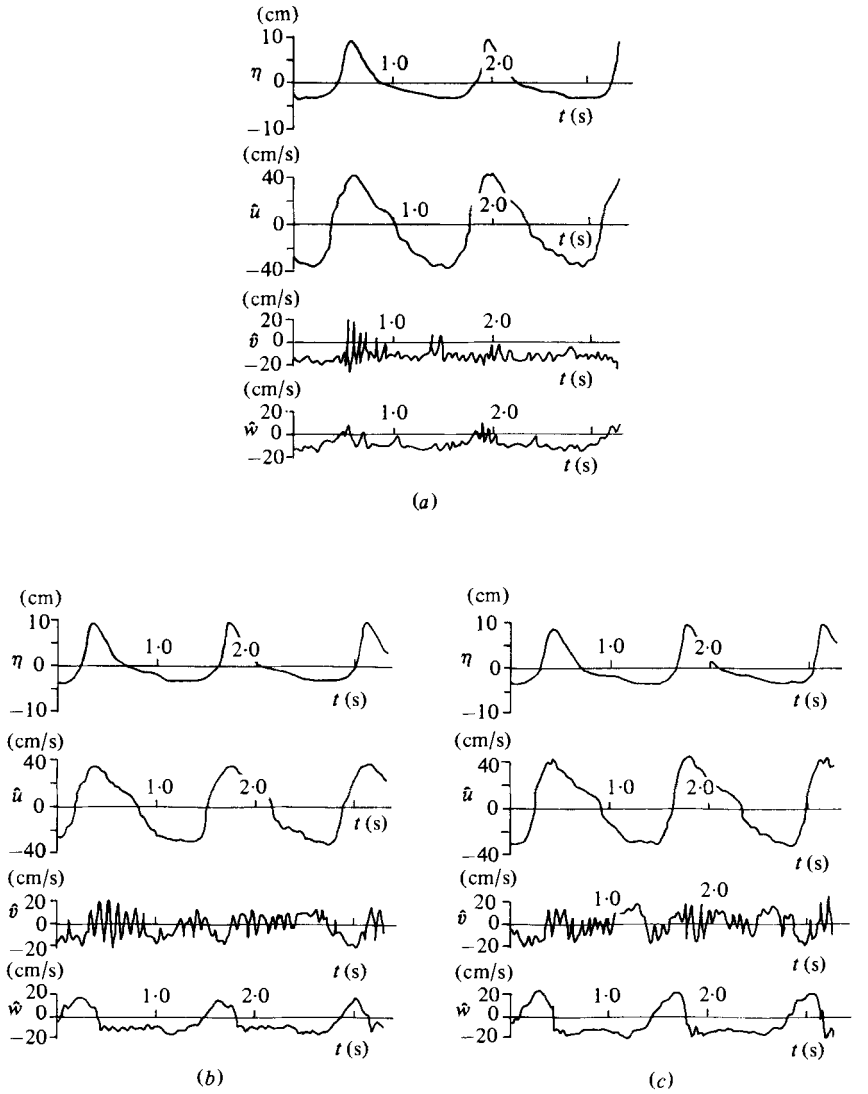

FIGURE 8. Time histories of η, $\hat{u}$, $\hat{v}$ and $\hat{w}$ at the wave-breaking point: (*a*) 2 cm above the horizontal step; (*b*) 8 cm above the horizontal step; (*c*) 2 cm below the wave trough.

at $x/L = 1{\cdot}0$, while figure 13 shows these spectra at $x/L = -0{\cdot}05$. It should be noted that the position at $x/L = -1{\cdot}0$ is in front of the horizontal step, whereas the position at $x/L = -0{\cdot}05$ is over the horizontal step, but of course it is in front of the breaking point. Thus it may be possible that the shoaling effect on the energy distribution at each frequency is given by comparing the power spectra in figure 12 with those in figure 13. Figure 12 shows that the energy of $\hat{u}$ and $\hat{w}$ is concentrated only at both the original primary-wave frequency, 0·7 Hz, and the first-higher-harmonic frequency, 1·4 Hz. The energy of $\hat{v}$ is, however, mainly concentrated at the primary frequency, but not at the first higher harmonic frequency. In fact, the second energy peak is near 1·0 Hz. At the first higher harmonic frequency, 1·4 Hz, there is a tiny energy peak, and the energy of $\hat{v}$ is distributed in a frequency range lower than the primary-wave

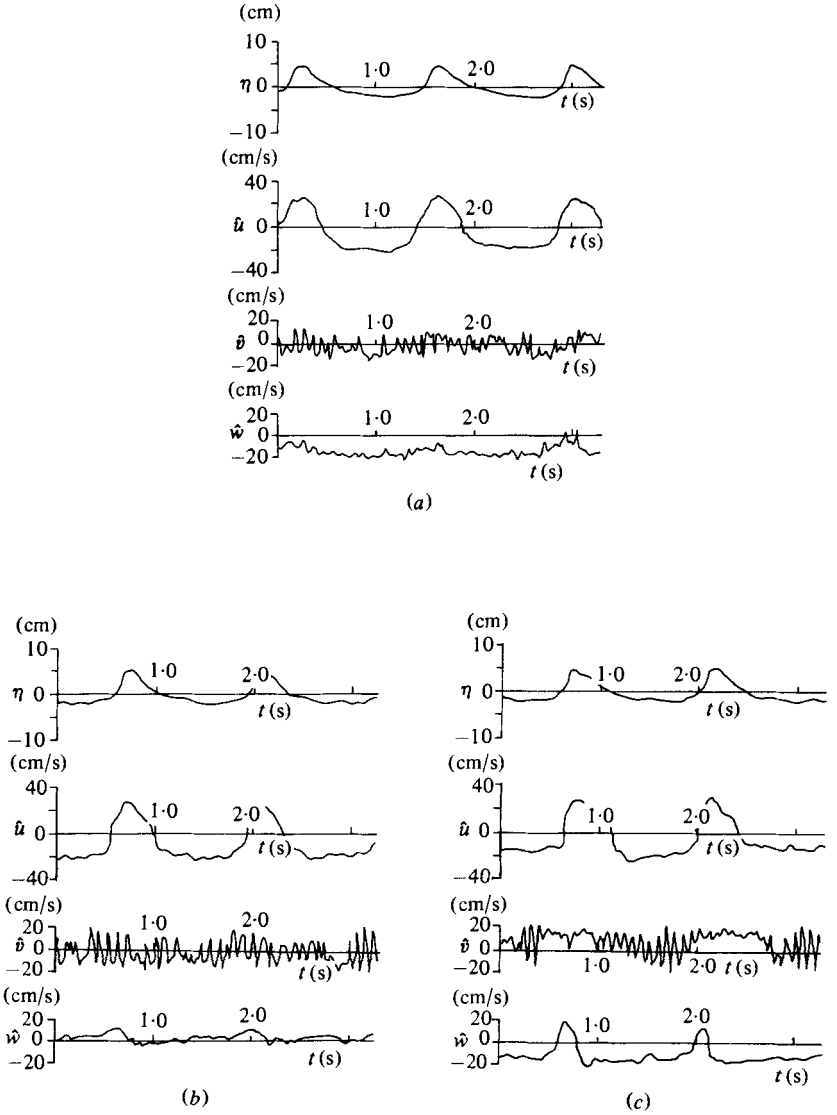

FIGURE 9. Time histories of η, $\hat{u}$, $\hat{v}$ and $\hat{w}$ behind the wave-breaking point. (*a*), (*b*), (*c*) as in figure 8.

frequency, as well as at the higher frequencies near 10·0 Hz. Note in figures 12–14 that the ordinate of the $\hat{u}$-spectrum starts from 10 cm^2/s, but that of the $\hat{v}$- and $\hat{w}$-spectra starts from 1·0 cm^2/s. On the one hand, figure 13 shows that, once the wave experiences the rapid shoaling from a constant tank bed to the horizontal step, the energy of $\hat{u}$ is distributed in the frequency range $0{\cdot}01 \lesssim f \lesssim 10{\cdot}0$, and the energy of $\hat{v}$ and $\hat{w}$ is distributed in the nearly full frequency range analysed here. Though the energy of $\hat{u}$, $\hat{v}$ and $\hat{w}$ is widely spread by the shoaling, it is characteristic that each of these spectra has strong peaks at the primary wave frequency and the first higher harmonic frequency. Hence it is considered that, even after experiencing relatively strong shoaling as in the present case, major wave frequencies in the original two-dimensional wave survive in both the longitudinal and vertical unsteady-flow

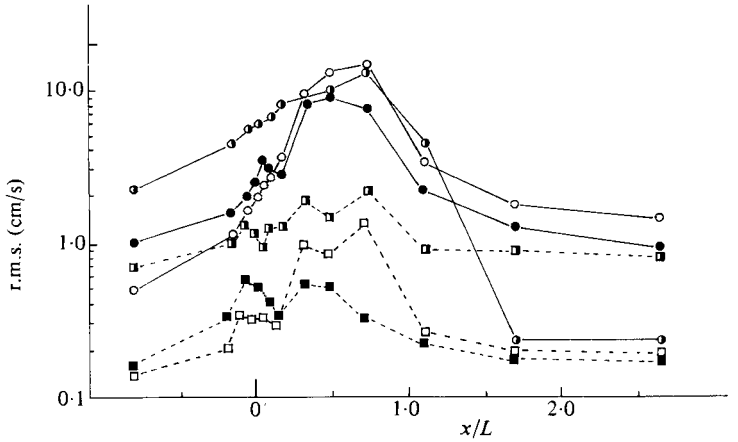

FIGURE 10. The r.m.s. value of u', v' or w' versus normalized distance x/L from the wave-breaking point. Phase average: ○, x; ◑, y; ●, z. Moving average: □, x; ◨, y; ■, z.

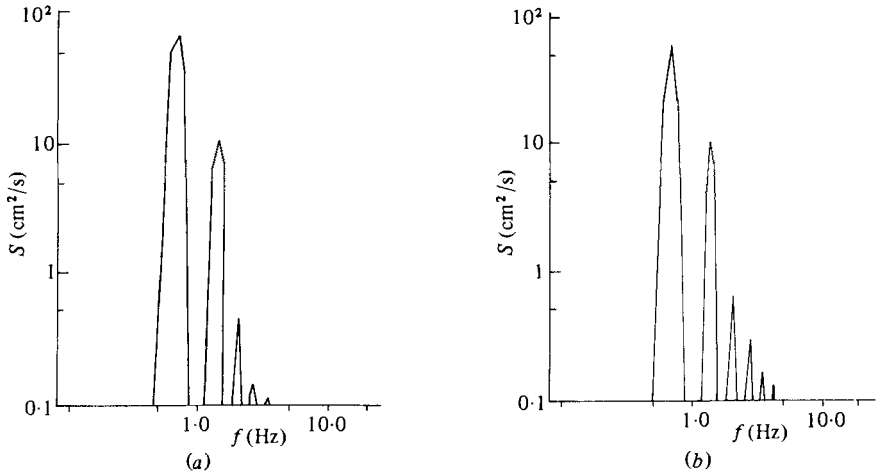

FIGURE 11. Power spectra of η, before shoaling and wave breaking.

components, and part of the original wave energy is transferred to the transverse unsteady-flow component and is located also at these major frequencies.

Figures 13 and 14 show power spectra just before the breaking point $x/L = -0{\cdot}05$ and just behind the breaking point $x/L = 0{\cdot}16$, respectively. Since both the positions are located over the horizontal step, the wave might not experience any shoaling between the two points, so that a comparison of the power spectra in figure 13 with those in figure 14 could provide the wave-breaking effect on the wave-energy distribution. Indeed, the comparison shows that the energy heights of $\hat{v}$ and $\hat{w}$ at the primary, the first higher harmonic and the second higher harmonic frequencies increase owing to the wave breaking. It may be noted in figure 14 that there is a fair amount of energy in the low-frequency range $f \lesssim 0{\cdot}5$ and a mild energy peak at $f \approx 0{\cdot}04$ appears in the spectra of both $\hat{v}$ and $\hat{w}$. However, except for these points, the difference between figures 13 and 14 in wave-energy distribution is relatively

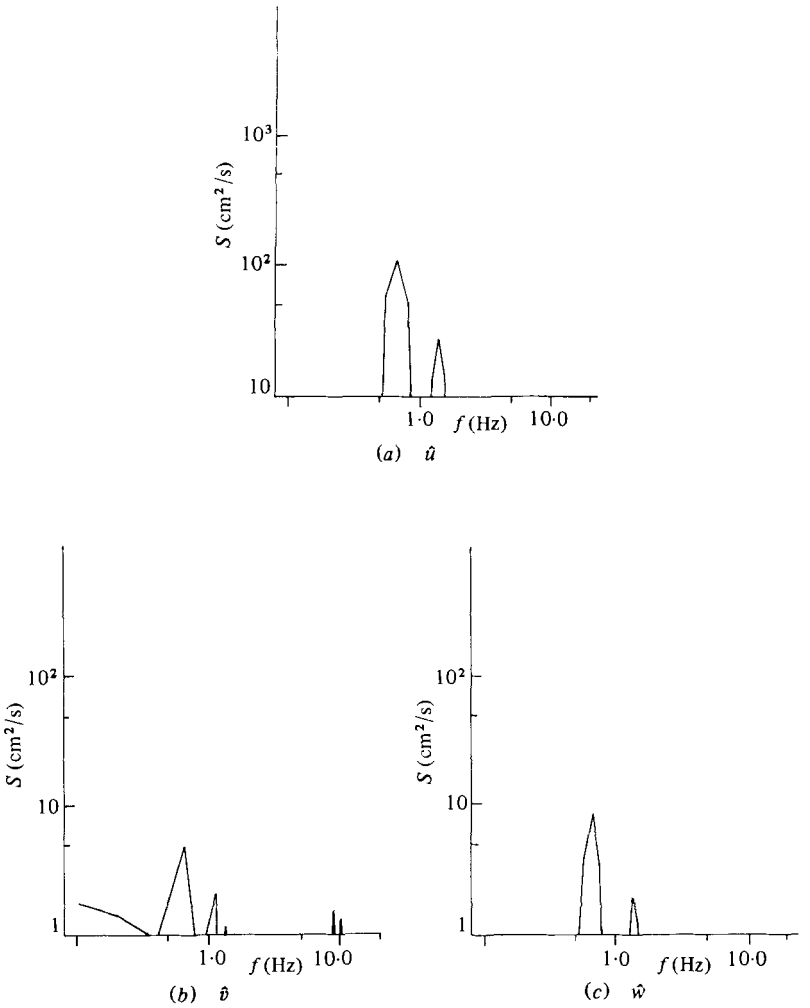

FIGURE 12. Power spectra of $\hat{u}$, $\hat{v}$ and $\hat{w}$, before shoaling and wave breaking.

small. Hence it can be concluded that the shoaling effect on the wave-energy distribution is much stronger than the wave-breaking effect.

Coherence. It is known that a coherence function denotes the correlation between two independent variables depending upon the frequency. Figure 15 shows $\eta\hat{u}$-, $\eta\hat{v}$- and $\eta\hat{w}$-coherences at $x/L = 0{\cdot}16$. It can be seen in figure 15(*a–c*) that, irrespective of the vertical position, $\eta\hat{u}$- and $\eta\hat{w}$-coherences become nearly 1·0 at the primary-wave frequency 0·7 Hz and at the first higher harmonic frequency 1·4 Hz. In contrast, figure 15(*b*) shows that $\eta\hat{v}$-coherence is smaller than 1·0 at both of these frequencies: at 2 cm below the wave trough (dotted line), the coherences at $f = 0{\cdot}7$ Hz and 1·4 Hz become 0·99 and 0·96 respectively, and at 2 cm above the horizontal step (solid line) their coherences are only 0·18 and 0·96 respectively.

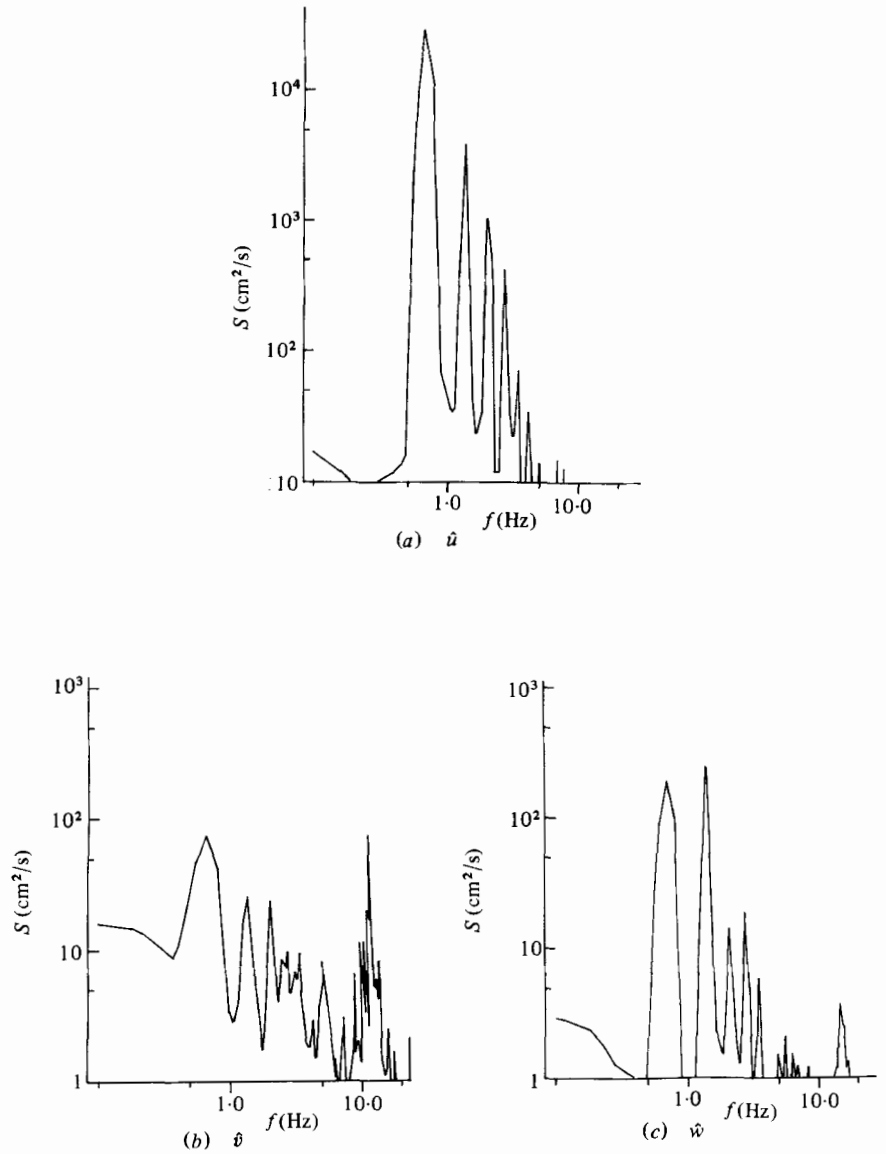

FIGURE 13. Power spectra of $\hat{u}$, $\hat{v}$ and $\hat{w}$ after the shoaling, but before the wave breaking. *not experiencing the wave breaking.*

5. Discussion

It may be worth noting in figure 12 (*b*) that there is only a tiny energy peak of $\hat{v}$ at the first higher harmonic frequency 1·4 Hz of the original wave. However, once the wave experiences shoaling, this becomes a conspicuous energy peak, as shown in figure 13 (*b*). Furthermore, figure 14 (*b*) shows that, through the wave-breaking process, the energy peak increases and becomes the second large one. This development of the energy peak may suggest that the energy distribution of the transverse unsteady flow component, generated either by the shoaling or wave breaking, is largely influenced by the frequencies in the original wave.

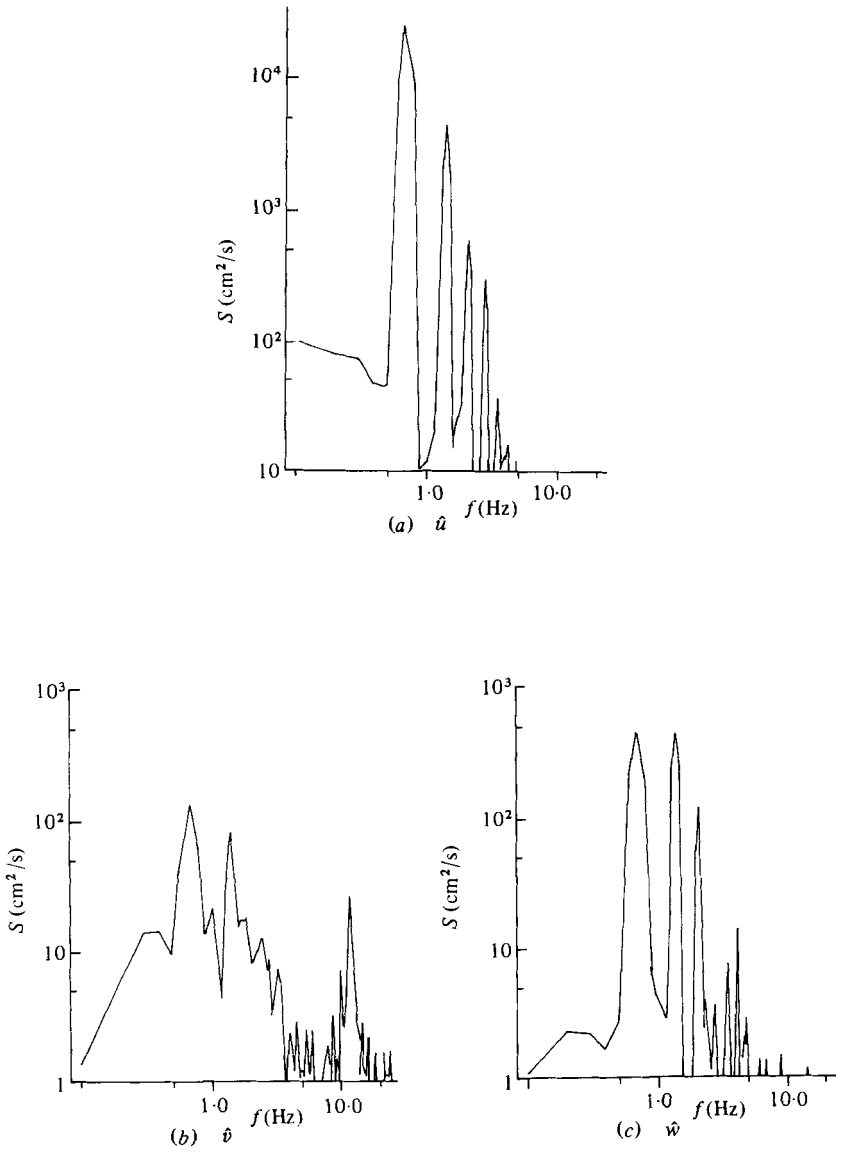

FIGURE 14. Power spectra of $\hat{u}$, $\hat{v}$ and $\hat{w}$ after shoaling and wave breaking.

Figures 13 and 14 show that the shoaling and wave breaking let the wave energy transfer to a frequency range lower than the primary original wave frequency (*negative cascade*) as well as to the higher-frequency range (*positive cascade*). It is seen in figures 13 and 14 that the shoaling and wave breaking provide the energy in the range $f \lesssim 0{\cdot}5$, but the former transfers the energy to a lower frequency range than does the latter. Figure 15 may suggest the same phenomenon as figures 13 and 14 associated with the 'negative cascade'. All of the coherences have fairly large values in the frequency range lower than the primary original wave frequency.

As has already been stated, there is as yet no appropriate definition of the turbulent fluctuation of the water-particle velocity in a breaking wave. It may therefore be worthwhile to point out some difficulties of the definition. Firstly, both the phase-

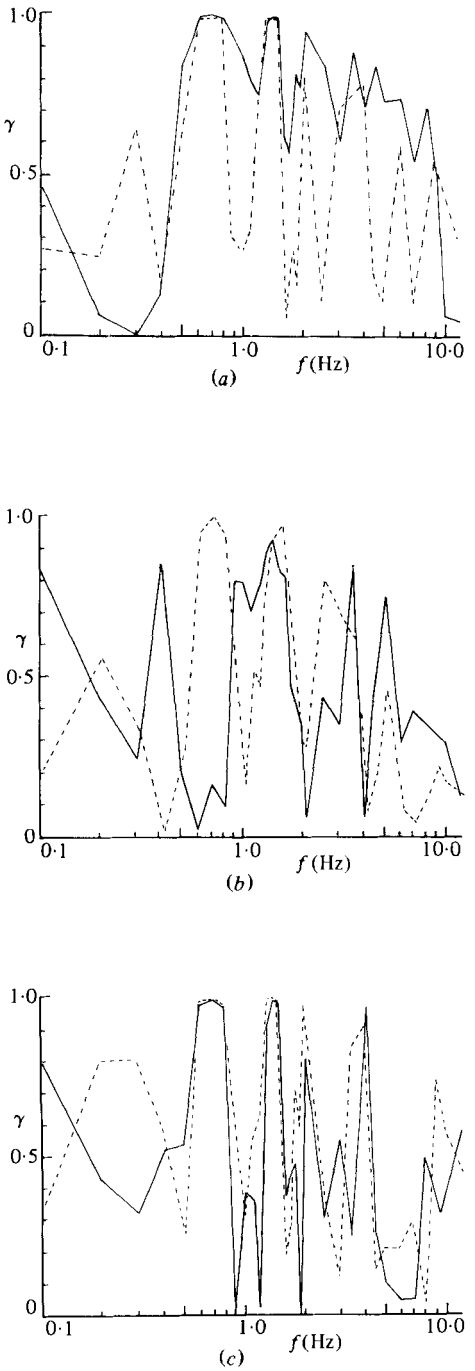

FIGURE 15. Coherences behind wave-breaking point at two different depths: (*a*) $\eta\hat{u}$-coherences; (*b*) $\eta\hat{v}$-coherences; (*c*) $\eta\hat{w}$-coherences; $x/L = 0{\cdot}16$. ——, 2 cm above the horizontal step; · · · ·, 2 cm below the wave trough.

and moving-average methods are considered to be valid only for oscillatory flows. It is clear from figure 10 that the behaviours of the r.m.s. value in the y-component are inconsistent with those of the other two r.m.s. values, and these could in part be attributed to the non-oscillatory nature of the transverse unsteady flow component. Secondly, the r.m.s. values depend upon the definition itself. Figure 10, for example, shows that these values by the phase-average method are nearly ten times those by the moving-average method. This must again be considered to be due to the incompleteness of the definition. However, a more-detailed discussion associated with the definition of turbulence in a breaking wave is beyond the scope of the present paper.

6. Conclusion

It is found that all three r.m.s. values in a plunging breaker become maximum at $x/L \approx 0{\cdot}7$. It is found that both velocity and r.m.s. value of the transverse-flow component newly generated by the shoaling and wave breaking become comparable to those of the other flow components in both longitudinal and vertical directions.

On the basis of the spectral analyses, it is found that major wave frequencies in both longitudinal and vertical flow components of the original two-dimensional wave survive, even after experiencing relatively strong shoaling and wave breaking, and part of the original wave energy is transferred to the transverse flow component and is located at the major frequencies. It is found that the majority of the higher harmonic frequency components (or turbulent fluctuations) are generated in the process of shoaling and that the wave breaking provides a relatively minor contribution to the generation. Finally, it is also found that, through the shoaling and wave-breaking processes, energy of the original wave is transported to a frequency range lower than the primary wave frequency (*negative cascade*), as well as to the higher-frequency range (*positive cascade*) in each flow component.

The author is grateful to Mr H. Koyama of Nagoya University for his assistance in the experiment and data analysis. The author's thanks are also due to Dr K. Iwata of Nagoya University for his help in the data analysis.

REFERENCES

ADEYEMO, M. D. 1970 Velocity field in the wave breaker zone. In *Proc. 12th Conf. Coastal Engng*, p. 435.

BATTJES, J. A. & SAKAI, T. 1981 Velocity field in a steady breaker. *J. Fluid Mech.* **111**, 421.

BLACKMAN, R. B. & TUKEY, U. W. 1958 *The Measurement of Power Spectra*. Dover.

BUB, F. L. 1974 Surf zone wave kinematics. M.Sc. thesis, Naval Postgraduate School, Monterey, California.

FÜHRBÖTER, A. & BÜSCHING, F. 1974 Wave measuring instrumentation for field investigations on breakers. In *Proc. Int. Symp. on Ocean Wave Measurement and Analyses*. A.S.C.E.

GALVIN, J. J. 1975 Kinematics of surf zone breaking wave; measurement and analysis. M.Sc. thesis, Naval Postgraduate School, Monterey, California.

HORIKAWA, K. & KUO, C. T. 1966 A study on wave transformation inside surf zone. In *Proc. 10th Conf. Coastal Engng*, p. 217.

IVERSEN, H. W. 1952 Waves and breakers in shoaling water. In *Proc. 3rd Conf. Coastal Engng*, p. 1.

LONGUET-HIGGINS, M. S. & COKELET, E. D. 1976 The deformation of steep surface waves on water. 1. A numerical method of computation. *Proc. R. Soc. Lond.* A **350**, 1.

MILLER, R. L. & ZIEGLER, J. M. 1964 The internal velocity field in breaking waves. In *Proc. 9th Conf. Coastal Engng*, p. 103.

MORISON, J. R. & CROOKE, R. C. 1953 The mechanics of deep water, shallow water, breaking waves. *Beach Erosion Board, Washington, D.C., Tech. Memo.* no. 40.

NAKAGAWA, T. 1982*a* Structural analyses and fluid dynamical considerations on tension thread flowmeter (in Japanese). In *Proc. 28th Japanese Structural Engng Symp.*, p. 65.

NAKAGAWA, T. 1982*b* A new instrument to measure three velocity components of water particles in breaking waves. Submitted to *J. Phys. E: Sci. Instrum.*

NAKAGAWA, T., IWATA, K. & KOYAMA, H. 1981 On characteristic of water particle velocity in breaking waves measured with tension thread flowmeter (in Japanese). In *Proc. 28th Conf. Japanese Coastal Engng*, p. 20.

PEREGRINE, D. E. & SVENDSEN, I. A. 1978 Spilling breakers, bores and hydraulic jumps. In *Proc. 16th Conf. Coastal Engng*, p. 540.

STEER, R. 1972 Kinematics of water particle motion within the surf zone. M.S. thesis, Naval Postgraduate School, Monterey, California.

THORNTON, E. B. 1968 A field investigation of sand transport in the surf zone. In *Proc. 11th Conf. Coastal Engng*, p. 335.

THORNTON, E. B., GALVIN, J. J., BUB, F. L. & RICHARDSON, D. P. 1976 Kinematics of breaking waves. In *Proc. 15th Conf. Coastal Engng*, p. 461.

THORNTON, E. B. & RICHARDSON, D. P. 1974 The kinematics of water particle velocities of breaking waves within the surf zone. *Naval Postgraduate School, Monterey, California, Tech. Rep.* NPS-58 TM 74011 A.

WALKER, J. R. 1969 Estimation of ocean wave-induced particle velocities from the time history of a bottom mounted pressure transducer. M.Sc. thesis, University of Hawaii.

WOOD, W. L. 1973 A wave and current investigation on the nearshore zone. Dept of Natural Science, Michigan State University, E. Lansing, Michigan.